IEEE Access
Multidisciplinary | Rapid Review | Open Access Journal

Received 16 March 2026, accepted 27 March 2026, date of publication 31 March 2026, date of current version 9 April 2026.

Digital Object Identifier 10.1109/ACCESS.2026.3679382

RESEARCH ARTICLE

A Wideband SSPP-Based Leaky-Wave Antenna Exploiting Quasi-Glide Symmetry for Millimeter-Wave Applications

EHSAN FAROKHIPOUR[1,2], (Graduate Student Member, IEEE), PENG-YUAN WANG[3], BENEDIKT SIEVERT[4], (Member, IEEE), ANDREAS RENNINGS[1,2], (Member, IEEE), AND DANIEL ERNI[1,2], (Member, IEEE)

[1]Laboratory for General and Theoretical Electrical Engineering (ATE), Faculty of Engineering, University of Duisburg–Essen, 47048 Duisburg, Germany
[2]Center for Nanointegration Duisburg–Essen (CENIDE), 47048 Duisburg, Germany
[3]Department of Electrical and Electronic Engineering, University of Nottingham Ningbo China, Ningbo 315100, China
[4]Department of Integrated Circuits, Fraunhofer Institute for High Frequency Physics and Radar Techniques (FHR), 53343 Wachtberg, Germany

Corresponding author: Ehsan Farokhipour (ehsan.farokhipour@uni-due.de)

This work was supported in part by the Deutsche Forschungsgemeinschaft (DFG, German Research Foundation) CRC/TRR 196 MARIE (Projects S03, C05) under Grant 287022738, in part by the Ministry of Culture and Science of the State of North Rhine-Westphalia (MKW NRW) through the Joint Project terahertz.NRW, and in part by German Federal Ministry of Education and Research (BMBF) through the 6GEM Research Hub under Grant 16KISK039.

ABSTRACT This article proposes a spoof surface plasmon polariton leaky-wave antenna (SSPP LWA) with independently suppressed open-stopband (OSB) and grating lobe for operation at millimeter-wave frequencies. The main operating section of the SSPP LWA consists of corrugated metallic strips loaded by a periodic arrangement of circular patches exhibiting quasi-glide symmetry, suppressing the OSB on the broadside. The OSB suppression is analyzed by accurately extracting the dispersion characteristic of the SSPP LWA. A theoretical method is proposed to predict the directional radiation patterns of the proposed LWA. Periodic LWAs suffer from the grating lobe at higher frequencies as the main beam scans toward the forward direction. To address this issue, we propose a modification of the unit cell radiation pattern. This increases the gain in the main beam direction while reducing it in the region where the grating lobe appears at higher frequencies. This behavior is achieved by employing asymmetrical slots within the circular patches. The simulated beam scans from -30° to $+46^\circ$ within a gain variation of 3.8 dB by varying the frequency from 55 GHz to 95 GHz. The simulated radiation efficiency over the entire band is above 77%. The measured beam scans from $+16^\circ$ to $+48^\circ$ with a maximum realized gain of 15 dBi in the frequency range of 75 GHz to 95 GHz. The simulated results agree well with the experimental data over a wide operating frequency range. The fabricated antenna on fused silica would be attractive for millimeter-wave radar and imaging systems.

INDEX TERMS Leaky-wave antennas, periodic structures, wideband, beam scanning, open stopband, grating lobe, millimeter-wave applications.

I. INTRODUCTION

Millimeter-wave frequencies have attracted considerable attention due to their applications in wireless communications and radar systems, such as navigation [1], wireless back-haul link [2], collision avoidance [3], target detection and tracking [4], and high-resolution imaging [5]. The millimeter-wave band has the merits of a relatively large bandwidth at each atmospheric window, offering substantial bandwidth and the ability to transmit multigigabit per second data rates over short distances. Moreover, the small free-space wavelength makes it easy to obtain miniaturization for the components and the antennas [6].

The leaky-wave antenna (LWA) is a cost-effective frequency-dependent beam-scanning antenna that can achieve a high gain and narrow beamwidth over a wide

The associate editor coordinating the review of this manuscript and approving it for publication was Jenny Mahoney.

frequency band. The advantages of LWA are their simple feeding structure, easy integration, and wide-angle beam-scanning capability [7], [8], [9], [10]. There are two types of LWAs: uniform LWA (U-LWA) and periodic LWA (P-LWA). In U-LWA, the main beam can only scan from the broadside to end-fire [11]. A P-LWA, on the other hand, consists of a slow waveguide structure that is periodically perturbed to change the slow wave into a fast spatial wave. The main beam in P-LWA scans from backward to forward direction [8].

However, P-LWAs suffer from two issues. The first is a gain degradation at the broadside due to the so-called open-stopband (OSB) phenomenon, where the input reflection increases and the radiation performance degrades due to interference effects in the radiated field between forward and back-reflected waves. The second is a grating lobe occurring in the backward direction at higher frequencies as the main beam scans toward the forward direction, where two space harmonics propagate simultaneously. Exploiting asymmetry in the unit cell structure is a solution already discussed in the literature to address the OSB issue [12], [13], [14]. Glide symmetry is one technique to close the OSB of an LWA due to its powerful ability to control transmission dispersion [15], [16], [17]. Tilting the unit cell's radiation pattern toward the array's main beam direction and maintaining the main beam without degradation at the lower frequency band is a solution to resolve the grating lobe issue [18], [19], [20]. The reported research in [12], [13], [14], [15], [16], [17], [18], [19], and [20] mainly focuses on suppressing either the OSB or the grating lobe. Therefore, it is still important to investigate methods to ensure that both OSB and the grating lobe are suppressed [21], [22]. Reference [21] presents two slot-array LWAs with different modulations. One suppresses the OSB, while the other suppresses the grating lobe. However, [21] does not achieve an independent suppression. Reference [22] proposes a P-LWA with a reverse dipole design to eliminate the OSB and the grating lobe. However, a complex simultaneous optimization of multiple parameters is necessary.

Various techniques, such as low-temperature co-fired ceramic (LTCC) and photolithography, have been adopted to meet the fabrication accuracy requirements for millimeter-wave applications. LTCC, as an integrated packaging substrate technology, involves numerous layers, leading to complex structural designs and generally higher costs [23]. In [23], two LWAs operating in the V and W-band were reported based on LTCC technology. The V-band LWA is fed by a coplanar waveguide (CPW), and the W-band single-port LWA is fed by a substrate-integrated waveguide (SIW). The V-band LWA achieves a beam-scanning range of 31°, while the W-band counterpart achieves a beam-scanning range of 22°.

Although conventional PCB reduces manufacturing costs, achieving high-performance antennas at high frequencies is difficult due to losses. Furthermore, the physical constraints imposed by the PCB technology limitations hinder the feasibility of designing PCB-based antennas for higher frequencies [24]. In [24], a PCB-based LWA based on SIW at the V-band is reported. The beam-scanning range is from $-28°$ to $+15°$. However, the performance was unsatisfactory and was not validated through measurements. In [7], a PCB-based LWA was proposed for the W-band frequencies. The maximal realized gain of 18 dBi was achieved through an electrically large antenna. Compared to conventional PCB technologies, photolithography can achieve a high resolution, allowing for the precise fabrication of intricate and miniaturized structures. Photolithography is a relatively cost-effective fabrication method, as it can be easily scaled for mass production, reducing manufacturing costs per unit [25].

Spoof surface plasmon polariton (SSPP) technology mimics the behavior of SPP at microwave and millimeter-wave frequencies [26]. SSPP has received much attention due to its highly confined EM waves, naturally broadband characteristics, and easily engineered dispersion for controllable scanning rate [27]. It can also be realized on a single-layer structure to further facilitate a full-space coverage and a better system integration compared to traditional SIW-based platforms [28]. However, a transition between SSPP waveguides (WGs) and conventional WGs, such as coplanar WGs (CPW) and microstrip lines, is necessary to facilitate integration with other millimeter-wave components [26], [27], [29], [30], [31], [32], [33]. These studies do not provide a detailed evaluation of the back-to-back connection performance of the transition. By introducing perturbations in the SSPP WG, leaky-wave radiation, namely SSPP leaky-wave antenna (SSPP LWA), can also be achieved [29], [30], [31], [32], [33], [34], [35], [36], [37]. In [36] and [37], SSPP LWAs were proposed based on 3D printing to operate in the V-band. In [36], a beam-scanning is achieved from $-39°$ to $-3°$ in the frequency range of 50 GHz to 75 GHz, showing a peak gain of 23.9 dBi. However, the antenna is not electrically compact. Although [37] has a compact structure, the LWA can generate a forward beam near the endfire direction.

Most SSPP-based devices rely on simplified dispersion characteristics calculated using the eigenmode solver of commercial software, which is not accurate enough [38]. The extraction of dispersion characteristics of the SSPP LWA to accurately analyze the radiation performance is still challenging due to the transition section that connects the conventional WG to the SSPP WG [39]. Although the recent SSPP LWA [39], published in 2024, employed an accurate dispersion extraction method, it has a limited beam scanning range from $-43°$ to $-11°$ with an electrically large transition circuit. Despite the recent progress, designing a high-performance millimeter-wave SSPP LWA that incorporates a compact, low-loss transition, a grating lobe suppression, and OSB suppression through an accurate dispersion characteristic extraction is essential.

This article proposes an SSPP LWA with a suppressed OSB and grating lobe to achieve beam-scanning for

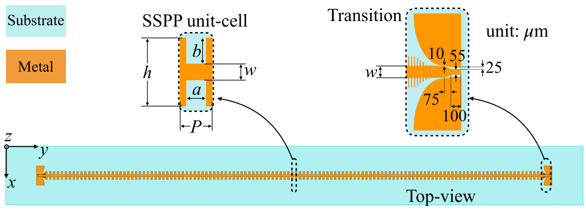

FIGURE 1. Configuration of the SSPP-TL (enlarged parts show the SSPP unit cell and the transition section from CPW to SSPP line). The dimensions are given in μm: $P = 250$, $h = 525$, $a = 150$, $b = 200$, $w = 125$.

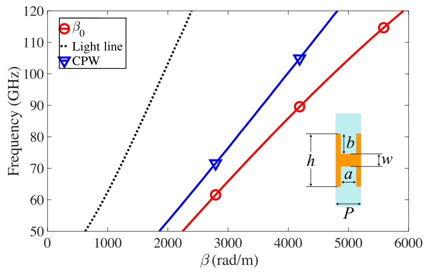

FIGURE 2. Dispersion diagram of the periodic SSPP-TL (the inset shows the SSPP unit cell).

millimeter-wave applications. Quasi-glide symmetry suppresses the OSB issue, and this suppression is analyzed through accurate extraction of the dispersion characteristics of the SSPP LWA. Furthermore, asymmetrical slots are used to improve the radiation coverage in the forward direction by tilting the unit cell radiation pattern. The simulated results show that exploiting the quasi-glide-symmetric structure with asymmetrical slots leads to continuous beam-scanning from $-30°$ to $+46°$ at operating frequencies ranging from 55 GHz to 95 GHz with a gain variation of 3.8 dB. The subsequent sections of the article are organized as follows. Section II presents SSPP-TL that feeds the parasitic patches. Section III presents the LWA and investigates the principle of leaky-wave radiation. Simulation results and a parametric study to examine the effect of three different design values on OSB and grating lobe suppression and proximity coupling enhancement are studied in section IV. Section V provides experimental validation, followed by the conclusion presented in Section VI.

II. SSPP TRANSMISSION LINE

Before investigating the LWA properties, the dispersion characteristics of a transmission line (TL) based on SSPP are studied, with a structure shown in Fig. 1. The length and width of the SSPP-TL are $L = 37$ mm and $W = 3.75$ mm. The general setup of the SSPP-TL consists of three regions, i.e., a main SSPP structure, a CPW, and a transition circuit (TC) between the SSPP structure and CPW. The SSPP structure consists of an array of sub-wavelength unit cells in the shape of a rectangular corrugated strip at both sides supporting a TM mode. The unit cells are printed on the upper side of a fused silica substrate with a thickness of $H = 300$ μm, a dielectric constant of 3.78, and a loss tangent of 0.0004.

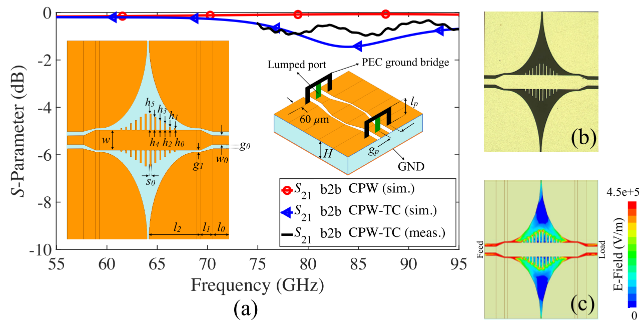

FIGURE 3. (a) Simulated S_{21} of the b2b transitions for CPW and CPW-TC, as well as the measured S_{21} of the b2b transition for CPW-TC (the inset shows the b2b configuration of CPW and CPW-TC). (b) Photographic image of the fabricated b2b CPW-TC. (c) E-field distribution of the designed b2b CPW-TC at 75 GHz. The dimensions are given in μm: $g_P = 75$, $l_P = 100$, $h_0 = 10$, $h_1 = 20$, $h_2 = 40$, $h_3 = 60$, $h_4 = 80$, $h_5 = 100$, $s_0 = 10$, $g_0 = 25$, $w_0 = 55$, $g_1 = 10$, $l_0 = 100$, $l_1 = 75$, $l_2 = 320$.

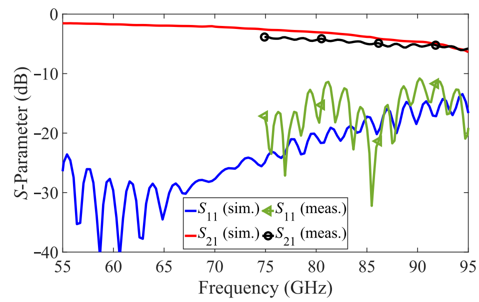

FIGURE 4. Measured (solid lines) and simulated (marked solid lines) scattering parameters of the proposed SSPP-TL.

A metallic layer is placed on the back side of the substrate as the ground plane. The thickness of the metallic top and bottom layers is 900 nm.

The dispersion diagram of the SSPP unit cell computed using ANSYS HFSS is depicted in Fig. 2. The fundamental mode of the SSPP unit cell is entirely below the light line, indicating guided slow-wave propagation in the SSPP structure along the y-direction. Fig. 3(a) shows the simulated S_{21} of the back-to-back (b2b) transitions of CPW and CPW-TC in the frequency range of 55 GHz to 95 GHz, as well as the measured S_{21} of the b2b transition of CPW-TC in the range of 75 GHz to 95 GHz. The configuration of the b2b transitions for CPW and CPW-TC is shown in the inset of Fig. 3(a) with detailed dimensions. The fabricated b2b transition of CPW-TC is shown in Fig. 3(b). To excite the CPW mode, a PEC bridge, located 60 μm from the edge of the structure, connects the two ground conductors, and a lumped port is utilized to excite the structure. This excitation method is chosen due to the actual on-wafer measurement scenario, where GSG probe tips excite the CPW from the top. The flaring ground dimensions of the TC influence the EM wave coupling to the corrugations, particularly at higher frequencies [40].

In our design, the electrical length of the CPW-TC is approximately $L_{TC} = 0.11\ \lambda_{68\mathrm{GHz}}$. The entering power is

TABLE 1. **Simulated insertion Loss (IL) of the CPW-TC and SSPP-TL.**

Structure	IL (dB)			IL per-mm (dB/mm)		
	55 GHz	75 GHz	95 GHz	55 GHz	75 GHz	95 GHz
b2b CPW-TC	0.19	0.47	0.69	–	–	–
SSPP-TL	1.54	2.61	6	–	–	–
SSPP structure	1.35	2.14	5.31	0.037	0.059	0.147

TABLE 2. **Measured insertion Loss (IL) of the CPW-TC and SSPP-TL.**

Structure	IL (dB)			IL per-mm (dB/mm)		
	55 GHz	75 GHz	95 GHz	55 GHz	75 GHz	95 GHz
b2b CPW-TC	N.A.	0.49	0.71	–	–	–
SSPP-TL	N.A.	3.85	6.1	–	–	–
SSPP structure	N.A.	3.36	5.39	N.A.	0.093	0.149

mainly guided through the central corrugations of the TC, indicating that a relatively small amount of power reaches the edges of the flaring ground. To examine this behavior, the E-field distribution at 75 GHz is shown in Fig. 3(c). Although S_{21} of the CPW-TC increases at higher frequencies, it is above -1.4 dB over the frequency range 55 GHz to 95 GHz. The TC is designed to attain a broadband momentum (i.e., wave vector respective propagation constant) and impedance matching between the TEM mode of the CPW and the TM mode of the SSPP structure at the expense of a radiation loss at high frequencies.

Fig. 4 shows the simulated scattering parameters of the final designed 37 mm long SSPP-TL in the range of 55 GHz to 95 GHz, as well as the measured scattering parameters in the range of 75 GHz to 95 GHz. The measurement result is almost consistent with the simulated one at the measured frequencies. The SSPP-TL is fed from the left side and terminated from the right side with a 50 Ω load. The simulated return loss shows good impedance matching in the frequency range of 55 GHz to 95 GHz, and the insertion loss increases with increasing frequency. The insertion loss of the SSPP-TL is composed of ohmic, dielectric, and radiation losses of the main SSPP structure and the mode-conversion loss of the CPW-TC.

To achieve the actual insertion loss of the main SSPP structure, the insertion loss of b2b CPW-TC should be subtracted from that of SSPP-TL. The simulated and measured insertion losses of b2b CPW-TC, SSPP-TL, and the main SSPP structure at different frequencies are given in Tables 1 and 2, respectively. For example, the simulated insertion loss of the SSPP-TL is 2.61 dB at 75 GHz. Since the insertion loss of the b2b CPW-TC is 0.47 dB, the insertion loss of the SSPP structure is 2.14 dB. Therefore, the attenuation of the SSPP structure is 0.059 dB/mm. It should be noted that the dielectric, conductor, and radiation losses of the flaring ground become relatively larger when the frequency increases. However, the S_{21} remains above -6 dB in the desired frequency band.

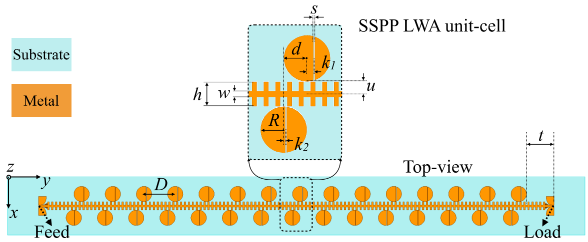

FIGURE 5. **Configuration of the proposed SSPP LWA (the enlarged part shows one unit cell of the antenna). The dimensions are given in μm: $R = 495$, $D = 2000$, $d = 500$, $s = 28$, $k_1 = 150$, $k_2 = 50$, $u = 207.5$, $t = 1750$.**

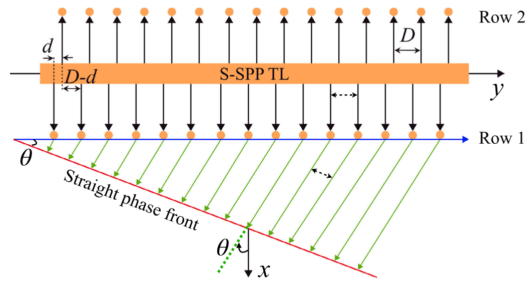

FIGURE 6. **Sketch of the proposed LWA equivalent model consisting of a center SSPP-TL and thirty parasitic perturbations (i.e, patches).**

III. DESIGN AND OPERATION PRINCIPLE

The configuration of the SSPP LWA is illustrated in Fig. 5. The proposed LWA consists of the SSPP-TL presented in Section II, loaded with two rows of metallic patches. The patches within the two rows are designed in a circular shape loaded with narrow slots, where the slots in the lower and upper rows are asymmetrically placed at different positions. The SSPP LWA is fed from the left side, and the right side is terminated with a 50 Ω load. The inset of Fig. 5 illustrates how a quasi-glide-symmetric structure forms the unit cell of the SSPP LWA. Each circular patch is flipped along the x-axis, shifted by distance d along the y-axis, and loaded by a differently positioned slot. The period of the LWA unit cell is D. The overall length and width of the LWA are $8.38\lambda_0$ and $0.85\lambda_0$, respectively. λ_0 is the free space wavelength at 68 GHz, indicating the broadside frequency.

As explained in the section II, the slow-wave of the SSPP structure cannot radiate. Therefore, the SSPP structure must be perturbed periodically to excite the leaky-wave radiation. When perturbations with period D are introduced into the SSPP structure, infinite space harmonics of the guided SSPP waves, according to the Floquet theorem, are excited. Here, we assume that the EM waves propagate along the y-direction in the SSPP-TL. Each generated space harmonic is characterized by the phase constant $\beta_n = \beta_0 + 2n\pi/D$, where β_0 is the phase constant of fundamental guided mode. Only negative n values can render fast space harmonics. To achieve a high radiation efficiency, the first fast space harmonic ($n = -1$) is selected for the proposed SSPP LWA, whose main beam direction can be calculated by

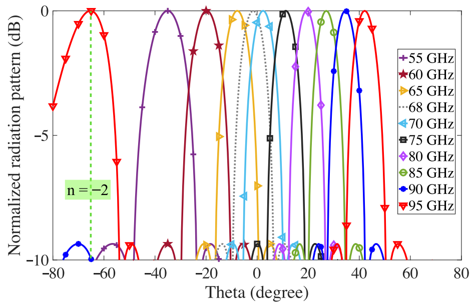

FIGURE 7. Predicted far-field radiation patterns at different frequencies based on (9).

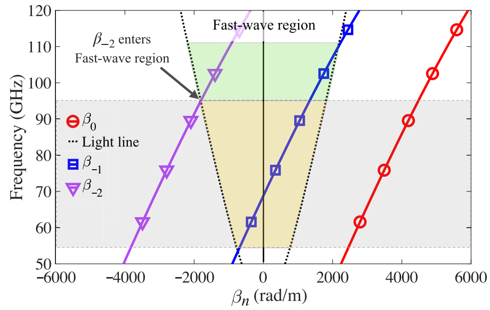

FIGURE 8. Dispersion curves of the SSPP LWA. The red curve is the fundamental dispersion curve of the SSPP unit cell. The blue and purple curves are for the first and second-order space harmonics of the SSPP LWA unit cell after applying the periodic perturbations.

$$\theta_{-1} = \sin^{-1}\left(\frac{\beta_{-1}}{k_0}\right) = \sin^{-1}\left(\frac{\beta_0 - 2\pi/D}{k_0}\right) \tag{1}$$

To ensure a single-harmonic radiation condition, the -1^{st} space harmonic should satisfy $-k_0 < \beta_{-1} < k_0$. In addition, we should also ensure that the -2^{nd} space harmonic behaves as a slow-wave ($\beta_{-2} = \beta_0 - 4\pi/D < -k_0$) in the desired frequency band. By solving the two single-harmonic radiation conditions, a suitable range of D can be obtained as

$$\frac{2\pi}{k_0 + \beta_0} < D < \min\left\{\frac{2\pi}{\beta_0 - k_0}, \frac{4\pi}{\beta_0 + k_0}\right\} \tag{2}$$

We provide a simplified model to facilitate the analysis as plotted in Fig. 6. First, EM waves are coupled from the SSPP-TL to the patches. Second, they are radiated through the parasitic perturbations into free space. In the first step, different phases are observed at various locations along the TL when EM waves propagate along the SSPP-TL. The offsets of the two adjacent elements are d and $D - d$ along the y-direction. Therefore, the phase differences and the wave range differences between the array elements along the y-direction can be written as [26] and [29]

$$\delta_1 = \beta_0\, d \tag{3}$$
$$\delta_2 = \beta_0\, (D - d) \tag{4}$$
$$\psi_1 = k_0\, d \sin\theta \tag{5}$$
$$\psi_2 = k_0\, (D - d) \sin\theta \tag{6}$$

where β_0 is the phase constant of the fundamental guided mode in the SSPP-TL, and θ is the main beam direction. The phases along the propagation direction can be expressed as

$$\Phi_1 = \psi_1 + \delta_1 = d\,(k_0 \sin\theta + \beta_0) \tag{7}$$
$$\Phi_2 = \psi_2 + \delta_2 = (D - d)\,(k_0 \sin\theta + \beta_0) \tag{8}$$

According to the antenna array principle [41], the beam direction can be calculated as

$$f_T(\theta) = f_1(\theta) + f_2(\theta) = 2\frac{\sin(\frac{N}{2}(\Phi_1 + \Phi_2))}{\sin(\frac{1}{2}(\Phi_1 + \Phi_2))} \tag{9}$$

where $f_1(\theta)$ and $f_2(\theta)$ are the directional patterns related to rows 1 and 2, respectively. $N = 15$ represents the number of patches on each side. In the design procedure, we consider $d = 0.5$ mm $= \lambda_g/4$, and $D = 2$ mm $= \lambda_g$ (where λ_g is the guided wavelength in the SSPP-TL at 68 GHz).

The theoretical calculation is used to prove the beam-scanning phenomenon. To do so, the feed amplitude of each array element is 1. The normalized far-field radiation pattern can be obtained using (9), as shown in Fig. 7. The main beam can be continuously scanned from backward to forward direction in the frequency range 55 GHz to 95 GHz. However, an unwanted grating lobe appears at 95 GHz. As evidenced by the dispersion curves depicted in Fig. 8, after applying periodic perturbations with period $D = 2$ mm, the -1^{st} space harmonic enters the fast-wave region at 55 GHz. At around 94.2 GHz, the -2^{nd} space harmonic enters the fast-wave region. This occurrence signifies that beyond the 94.2 GHz threshold, the -2^{nd} space harmonic exhibits grating lobe radiation in the backward direction, as predicted in Fig. 7.

IV. FULL WAVE SIMULATION RESULTS

All the simulations to design and optimize the proposed SSPP LWA are conducted using ANSYS HFSS. In this study, two different types of parasitic elements, i.e., solid circular patches with and without slots, are investigated. We call the LWA loaded by circular patches without slots LWA 1 and the one with optimally placed asymmetrical slots LWA 2. To highlight the effect of slots at higher frequencies, the unit cell radiation patterns and simulated electric field distributions of LWA 1 and LWA 2 at different frequencies are shown in Fig. 9. The unit cell radiation patterns demonstrate an approximately comparable performance at lower frequencies, such as 55, 60, 70, and 80 GHz. However, the unit cell radiation pattern of LWA 2 has stronger radiation in the main lobe direction and weaker radiation in the grating lobe region at higher frequencies.

At 95 GHz, according to the Floquet Theorem, after introducing periodic perturbations, the beam direction of the -1^{st} and -2^{nd} space harmonics is toward $+46°$, and $-57°$. As shown in Fig. 9(f), the unit cell of LWA 2 has a unique radiation pattern tilted toward the main beam direction with less radiation in the backward direction, which is achieved by optimizing the position of the slots. To provide a better insight

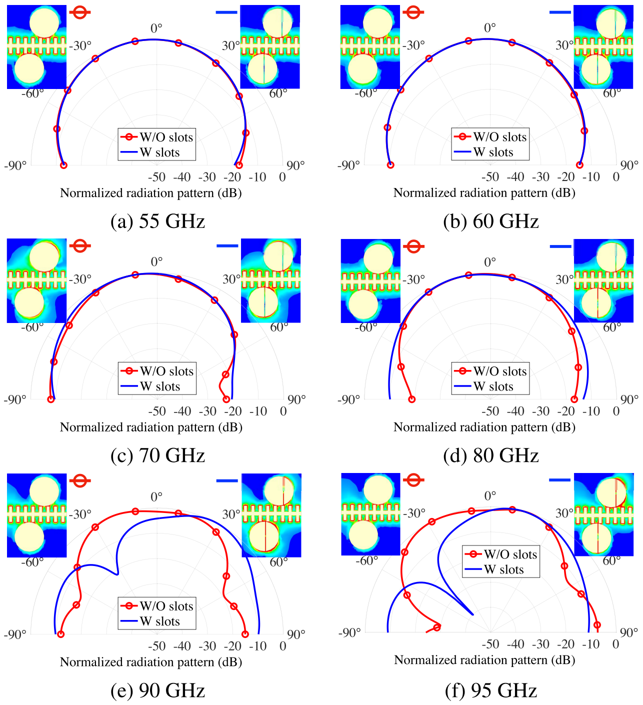

FIGURE 9. Concept of grating lobe suppression using beam tilting of the radiation pattern. (a)–(f) show the normalized unit cell radiation patterns and electric field distributions of LWA 1 (solid with marker) and LWA 2 (solid) at different frequencies: 55, 60, 70, 80, 90, and 95 GHz.

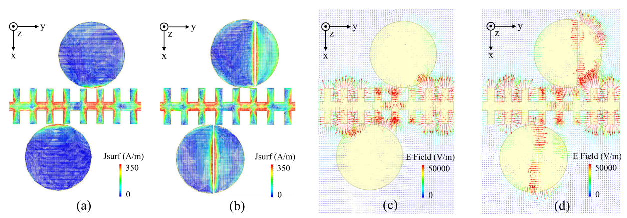

FIGURE 10. Simulated surface current and electric field distributions at 95 GHz on the unit cell of (a), (c) LWA 1 and (b), (d) LWA 2, respectively.

into the effect of the asymmetrical slots, the simulated current distribution of the unit cell of LWA 1 and LWA 2 at 95 GHz is shown in Fig. 10(a) and (b). In the unit cell of LWA 1, the current distribution is concentrated near the edges of the lower and upper patches close to the SSPP-TL.

However, the slots in the unit cell of LWA 2 significantly change the current distribution in the patches. The current distribution is concentrated along the edges of the slots, particularly near the openings. The surface current on the upper patch is stronger toward the side edge than that on the lower patch. This behavior can be attributed to the asymmetrical positioning of the etched slots. The electric field distribution of the LWA 1 and LWA 2 at 95 GHz is also given in Fig. 10(c) and (d). The radiating field vectors in LWA 1 are concentrated around the SSPP-TL and inner edges of the radiators. However, slots in LWA 2 create a strong resonance, increasing the effective radiating area. The radiating electric field of LWA 2 is also asymmetrically concentrated at the outer edges of the upper and lower

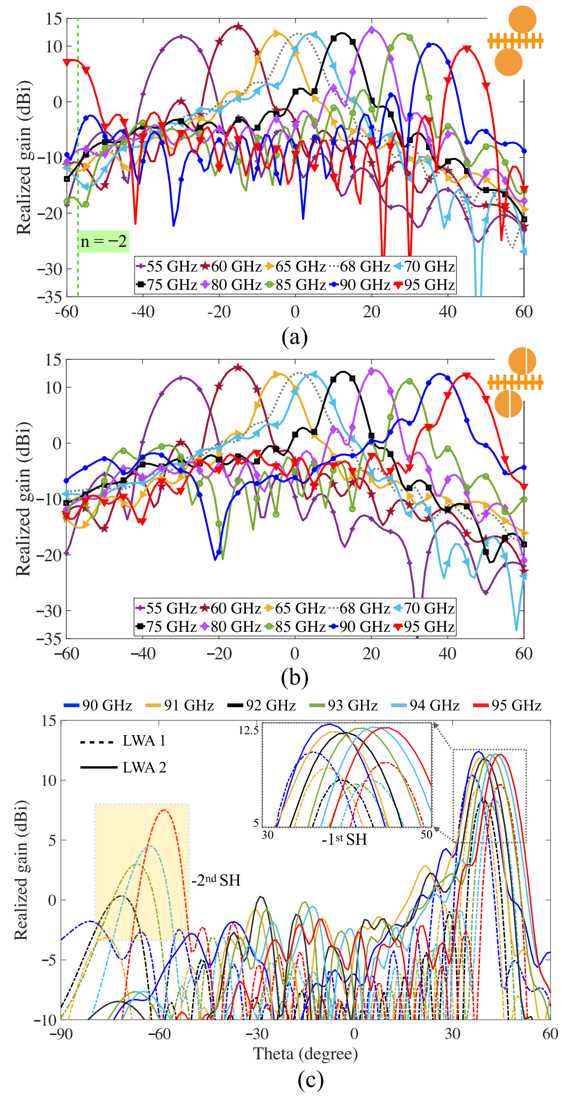

FIGURE 11. Simulated radiation patterns in the *yz*-plane for (a) LWA 1 and (b) LWA 2. (c) Comparison between the radiation patterns of LWA 1 and LWA 2 at frequencies between 90 GHz and 95 GHz.

radiators, with a stronger intensity on the upper radiator due to the differently positioned slots. As a result, asymmetrical slots tilt the unit cell radiation pattern toward the -1^{st} space harmonic and reduce it in the region where the grating lobe appears at higher frequencies.

The radiation patterns of LWA 1 in the *yz*-plane are shown in Fig. 11(a). The slight deviation in the simulated radiation directions compared to the predicted ones in Fig. 7 is due to the ideal assumption during the theoretical analysis. The unit cell radiation and mutual coupling between adjacent patches are neglected. Meanwhile, the excitation amplitudes of the patches differ due to energy leakage along the SSPP-TL. The radiation patterns of LWA 2 in the *yz*-plane are shown in Fig. 11(b) to display the scanning range improvement with grating lobe suppression in the full-array level at higher frequencies by tilting the unit cell radiation after adding slots. As shown in Fig. 11(c), the -2^{nd} space harmonic

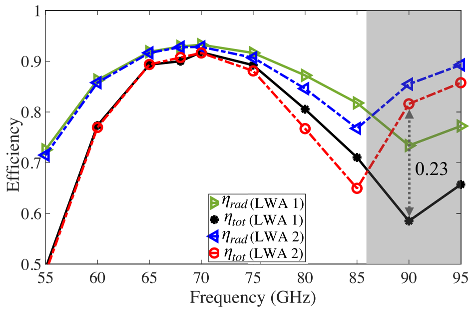

FIGURE 12. Simulated radiation and total efficiencies (η_{rad} and η_{tot}) of the SSPP LWA 1 and LWA 2.

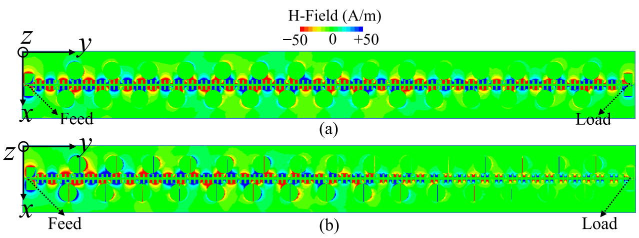

FIGURE 13. Simulated H_z distribution at 95 GHz for (a) SSPP LWA 1 and (b) SSPP LWA 2.

of LWA 1 gradually appears in the backward direction. However, it can be seen that the main beam of LWA 2 exhibits a higher gain than that of LWA 1, while also effectively suppressing the grating lobe. It is noted that, based on the dispersion diagram in Fig. 8, the -2^{nd} space harmonic enters the multimode leaky region at 94.2 GHz. However, the simulated radiation patterns show this occurs at slightly lower frequencies. This frequency shift can also be attributed to the fact that transitions, elemental radiation, and coupling effects are not considered in the dispersion diagram.

Fig. 12 shows the simulated radiation efficiencies (η_{rad}) and total efficiencies (η_{tot}). The total efficiency is calculated by $\eta_{tot} = (1 - |S_{11}|^2 - |S_{21}|^2)\eta_{rad}$ to remove the effects of mismatch and non-radiated power at the end of the LWA. Low η_{tot} at lower frequencies around 55 GHz can be associated with the higher value of S_{21}. At frequencies above 85 GHz, around 23% total efficiency enhancement is achieved by introducing slots into the circular patches, as shown in Fig. 12. Both η_{rad} and η_{tot} for LWA 2 increase at higher frequencies. These findings indicate that introducing asymmetrical slots extends the scanning range by approximately 10° in the forward direction.

To further study the influence of the slots, Fig. 13 shows the computed magnetic field H_z at 95 GHz. A confined surface mode propagation along the SSPP-TL is observed. The field distribution is periodically bouncing between the two sides of the H-shaped unit cells. The patches are located at the positions with the maximum magnetic field to maximize coupling. LWA 1 delivers more power to the second port instead of radiating into free space. Compared with patches without slots, resonance in the slots appears at

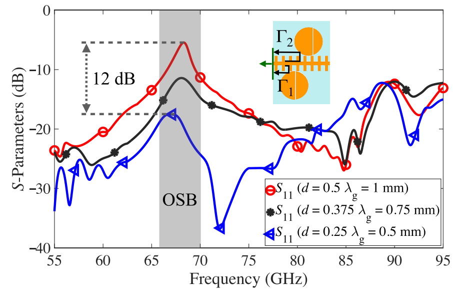

FIGURE 14. Simulated scattering parameters of LWA 2 for different values of d. The gray shaded area indicates the stopband.

higher frequencies, resulting in a constructive superposition in the far-field radiation at 95 GHz.

A. PARAMETRIC STUDY

Three parameters are selected for adjustments to further evaluate the performance of the proposed SSPP LWA 2: (1) the center-to-center distance of the lower and upper patches in one LWA unit cell (referred to as d), (2) center of the patches to the centers of the lower and upper slots (referred to as k_1 and k_2) and (3) the coupling distance between the center corrugated SSPP-TL to the lower edge of the parasitic patches (referred to as u). This parametric study aims to investigate the influence of d on OSB suppression and the effect of u on the proximity coupling enhancement.

1) INFLUENCE OF *D* ON OSB SUPPRESSION

Fig. 14 depicts the reflection coefficient of the SSPP LWA 2 with different distances d to suppress the OSB. In theory, to eliminate the reflected power back to the input port, the two components of the reflected wave from each parasitic patch in the SSPP LWA 2 unit cell must cancel each other out. As shown in Fig. 14, in the case of $d = 0.5\lambda_g$, there is a strong OSB in the range of 67.1 GHz to 69.5 GHz. However, the OSB is suppressed when the value of d toward $0.25\lambda_g$ is reduced. The quarter wavelength separation ($d = 0.25\lambda_g$) ensures that both components of the reflected wave are out of phase, resulting in an improvement of approximately 12 dB in S_{11}. It should be noted that the dispersion curves shown in Fig. 8 are derived using the eigenmode solver under the assumption that the SSPP-TL consists of an infinite series of periodic unit cells, without considering the mutual coupling and the finite size of the structure. However, LWA is based on a finite SSPP-TL surrounded by two rows of parasitic patches and placed between two transition structures. Fig. 15 shows a general cascade network of SSPP LWA unit cells sandwiched between two transitions, whose effect should be excluded for accurate dispersion characteristics [39].

To analyze the OSB suppression more accurately, we calculate the phase and attenuation constants of the -1^{st} space harmonic versus frequency using the calibration technique proposed in [42]. Here, the dispersion characteristics of the SSPP LWA are extracted from the simulated S-parameters.

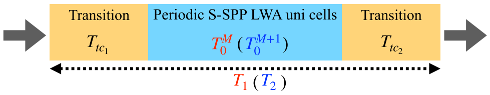

FIGURE 15. Schematic of an equivalent cascaded network of SSPP LWAs.

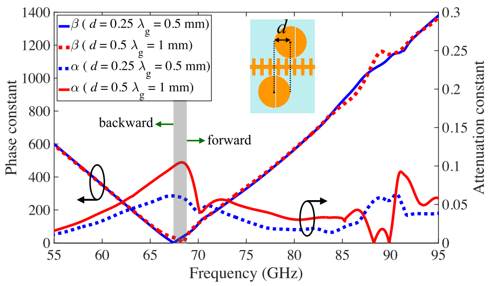

FIGURE 16. Calculated phase and attenuation constants, namely α and β_{-1}, of the LWA 2 versus frequency by the calibration technique.

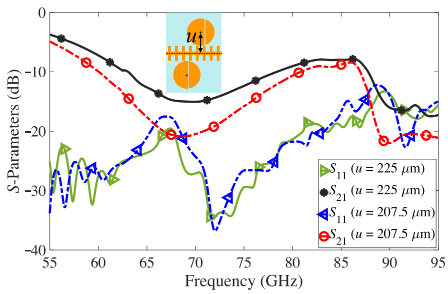

FIGURE 17. Simulated scattering parameters of LWA 2 for different values of u. A smaller u increases the proximity coupling.

Two structures with different numbers of unit cells, whose lengths are different in one SSPP LWA unit cell, are considered to obtain the dispersion curve of a single SSPP LWA unit cell. $\mathbf{T}_1$ and $\mathbf{T}_2$ are considered as the transmission matrices of the two structures, and can be represented as

$$\mathbf{T}_1 = \mathbf{T}_{tc_1}\mathbf{T}_0^M\mathbf{T}_{tc_2}, \qquad \mathbf{T}_2 = \mathbf{T}_{tc_1}\mathbf{T}_0^{M+1}\mathbf{T}_{tc_2} \tag{10}$$

where $\mathbf{T}_{tc_1}$ and $\mathbf{T}_{tc_2}$ are the transmission matrices of the left and right-hand sides of both transition structures, respectively. $\mathbf{T}_0^M$, $\mathbf{T}_0^{M+1}$ are the transmission matrices of the structure with M and $M+1$ SSPP LWA unit cells, respectively. By multiplying the matrices $\mathbf{T}_1^{-1}$ and $\mathbf{T}_2$, it can be calculated that the matrix $\mathbf{T}_1^{-1}\mathbf{T}_2$ and $\mathbf{T}_0$ are similar. $\mathbf{T}_0$ is the transmission matrix for each SSPP LWA unit cell. The eigenvalue of the matrix $\mathbf{T}_1^{-1}\mathbf{T}_2$ is computed by solving

$$\det\Big((\mathbf{T}_1^{-1}\mathbf{T}_2) - \lambda\mathbf{I}\Big) = 0, \qquad \lambda = e^{\gamma D} \tag{11}$$

where $\gamma = \alpha + j\beta_{-1}$ and D are the complex propagation constant and the period of the SSPP LWA unit cell, respectively. α and β_{-1} can be extracted from the computed eigenvalue of the matrix $\mathbf{T}_1^{-1}\mathbf{T}_2$. Fig. 16 shows the dispersion graph with two different values of d. The OSB phenomenon for $d = 0.5\lambda_g$ is found in the vicinity of 68 GHz (broadside direction), which results in the summation of the internal reflections in the structure, as evidenced in Fig. 14. However,

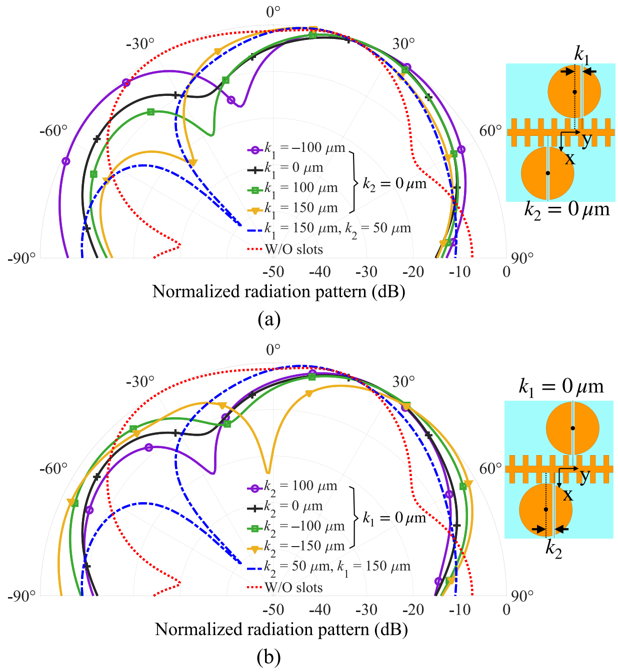

FIGURE 18. Normalized unit cell radiation pattern of the proposed LWA at 95 GHz for (a) a fixed $k_1 = 0$ μm with varying k_2, and (b) a fixed $k_2 = 0$ μm with varying k_1.

in the case of $d = 0.25\lambda_g$, the attenuation constant decreases, and the return phase of the reflections between the upper and lower parasitic patches cancel each other out, which leads to OSB suppression in the broadside direction. It should be noted that the design procedure for OSB suppression and the grating lobe suppression are completely independent. OSB suppression is enabled by the glide-symmetry configuration, while asymmetrically positioned slots achieve grating lobe suppression with minimal impact on the OSB behavior.

2) INFLUENCE OF U ON PROXIMITY COUPLING

Fig. 17 depicts the scattering parameters of the SSPP LWA 2 for different u. The variation in S_{21} between the two cases indicates that when the patches are positioned closer to the center SSPP-TL, S_{21} is reduced, resulting in a stronger coupling between the patches and the center line. This behavior is predictable depending on the proximity of the patches to the center of the SSPP-TL. Since the guided waves of the SSPP-TL are confined, the EM coupling between the patches and the center line decreases by moving the patches away from the line.

3) INFLUENCE OF K_1 AND K_2 ON GRATING LOBE

Fig. 18 shows the normalized radiation pattern of the antenna unit cell at 95 GHz, illustrating a parametric study of the slot positions to achieve grating lobe suppression at the array level. The study investigates the effect of varying the distances k_1 and k_2, which are the distances between the center of the upper and lower slots to the center of the patches. The parametric study starts with circular patches

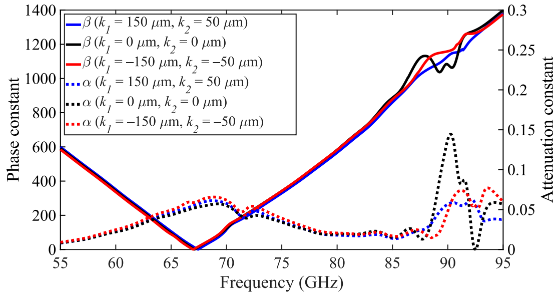

FIGURE 19. Calculated phase and attenuation constants of the proposed LWA with different slot placements.

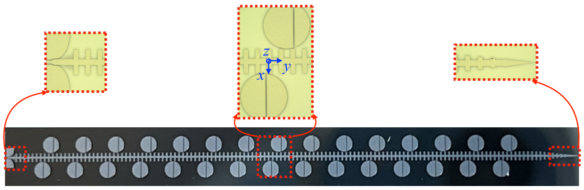

FIGURE 20. Photographs of the on-wafer antenna prototype (enlarged parts from left to right show the transition from CPW to SSPP unit cell, the unit cell of the SSPP LWA 2, and a tapering end from the SSPP structure).

without slots as a baseline to establish the reference radiation pattern, as shown in the red-dotted highlighted curve. Next, slots are etched into the patches with varying k_1 and k_2 to increase the radiation towards the main beam direction and reduce it in the region where the grating lobe appears at 95 GHz.

In the state of symmetrical slots at the center of the patches with $k_1 = k_2 = 0\ \mu$m, the radiation in the main beam direction is tilted, as illustrated in the black curve. However, the radiation of the unit cell towards the -2^{nd} space harmonic of the LWA is not reduce, which means that the grating lobe cannot be mitigated. As a next step, k_1 and k_2 are considered to be swept to find a potential case with a minimum unit cell radiation towards the -2^{nd} space harmonic. When k_2 is fixed at 0 μm and the upper slot is shifted from the left side of the patch center to the right, the null in the radiation diagram shifts toward the grating lobe region at 95 GHz. Similarly, when k_1 is fixed at 0 μm and the lower slot is shifted from left to right, the null also shifts toward the grating lobe direction. Consequently, the combined setting $k_1 = 150\ \mu$m and $k_2 = 50\ \mu$m produces a deeper null positioned closer to the grating lobe region at 95 GHz, which is selected as the final design.

Fig. 19 shows the dispersion curves for three different slot placements. It is observed that the OSB suppression controlled by the parameter d is independent of the grating lobe suppression mechanism introduced by the position of the asymmetrical slots. The extracted curves show nearly identical behavior for all cases around the broadside direction. This supports the idea that d is the most important parameter controlling OSB suppression, while the position of the asymmetric slots mainly affects radiation characteristics around the grating lobe region with minimal impact on OSB suppression.

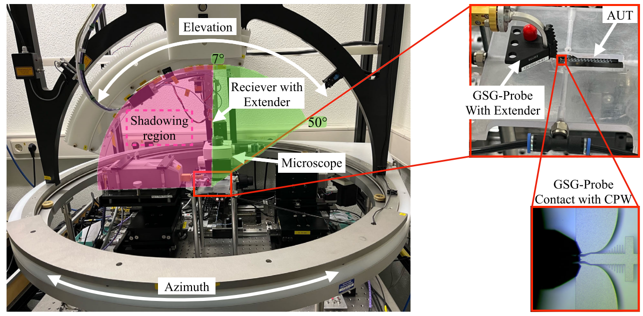

FIGURE 21. On-wafer hemispherical antenna measurement system for far-field radiation pattern measurements (the enlarged parts show a zoom-in view of the antenna under test (AUT), and a microscopic view of the GSG probe connection to the CPW line of the antenna) [44].

V. EXPERIMENTAL VALIDATION

In traditional LWAs, a load is typically applied at the rear port to dissipate the transmitted power. However, this matching load increases the cost in the high-frequency band. Here, a tapering end from the SSPP structure is used to eliminate the requirement for a terminating matching load. The tapering end improves reflection performance by gradually matching the SSPP line impedance to that of free space. This smooth impedance transition minimizes abrupt reflections, reducing the reflection losses. A single-port prototype of the LWA 2 with a tapered end termination was manufactured using photolithography and measured to verify the analytical and numerical results. To ensure consistency, the numerical simulations in this section were performed using the identical single-port configuration with the tapered end termination. Photographs of the manufactured antenna in the top view are shown in Fig. 20. The antenna is realized on a fused silica wafer with a thickness of 300 μm. The total footprint of the antenna is $8.38 \times 0.85\lambda_0^2$. For experimental validation of the proposed single-port SSPP LWA 2, an on-wafer measurement setup is employed.

Fig. 21 shows the on-wafer measurement together with the hemispherical millimeter-wave/THz antenna measurement setup to measure the return loss and far-field radiation pattern of the proposed antenna [43]. A ground-signal-ground (GSG) probe with 75 μm pitch feeds the antenna via its CPW TL, enabling a precise and controlled connection. A strategic approach is utilized to characterize the proposed antenna. A polycarbonate chuck with a relative permittivity of 2.5 is selected to facilitate the measurement process. A rectangular hole, slightly larger than the antenna dimensions, was crafted into the substrate chuck. This cavity is a dedicated space to place the antenna, which is fixed on the polycarbonate chuck using three vacuum holes. Combining the tailored air cavity for antenna placement and implementing vacuum holes maintains the antenna stability during the GSG connection.

The practical limitations of our measurement facilities have limited the antenna characterization to the W-band frequencies from 75 GHz to 95 GHz, and an elevation range from 0° to 50°. Precisely speaking, the scattering parameter characterization is restricted to the W-band because of the

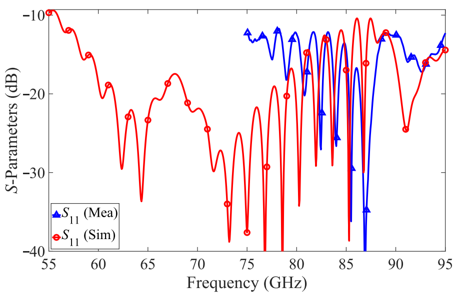

FIGURE 22. Measured and simulated results of the reflection coefficient of the proposed antenna.

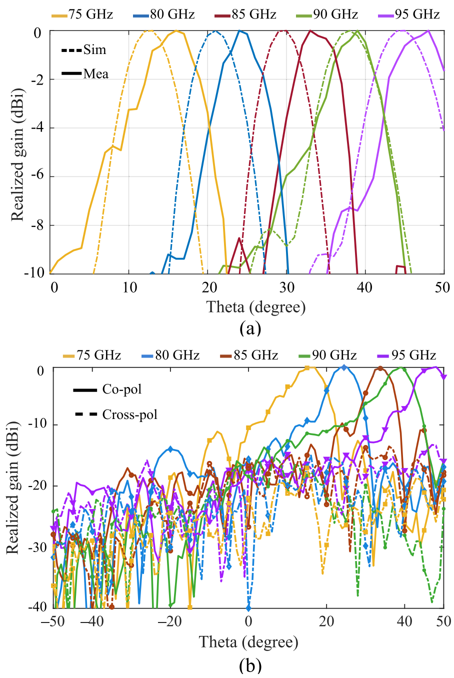

FIGURE 23. (a) Normalized measured and simulated radiation patterns of the proposed antenna in *yz*-plane at different frequencies. (b) Normalized measured co-pol and cross-pol radiation patterns at different frequencies.

lack of equipment, such as a GSG probe and an extender for the V-band. Additionally, a full space far-field characterization is impossible and limited to the forward direction owing to the physical shape and position of the GSG probe and its shadowing effect in the backward direction [44], [45]. For experimental S_{11} characterization, a VNA (R&S ZNA43) with a millimeter-wave VNA extender (R&S ZC110) is used. Fig. 22 shows the simulated and measured return loss of the SSPP LWA. Simulated S_{11} indicates a broadband impedance matching from 55 GHz to 95 GHz. The measured S_{11} is below −10 dB in the frequency range of 75 GHz to 95 GHz, which shows an acceptable return loss and good power acceptance. The deviation between the simulated and measured results at lower frequencies can be attributed to the absence of the GSG probe body in the simulation model. The agreement between the simulated and measured S_{11} from 80 GHz to 95 GHz further confirms the accuracy of the design, fabrication, and measurement processes.

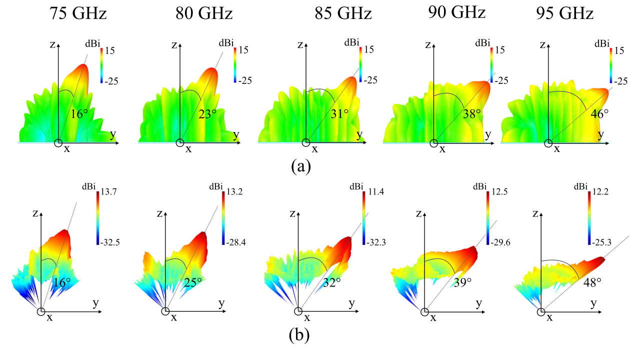

FIGURE 24. (a) Simulated and (b) measured 3D realized gain patterns of the proposed antenna in the *yz*-plane at different frequencies.

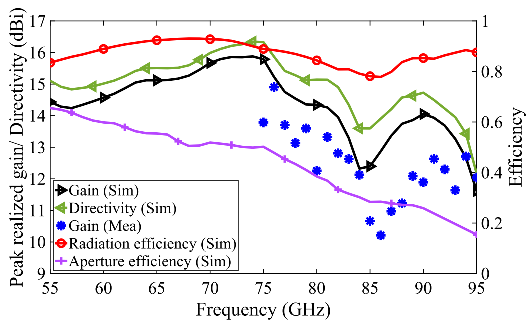

FIGURE 25. Measured and simulated maximum peak realized gain, along with the simulated directivity, radiation efficiency, and aperture efficiency of the proposed antenna versus frequency.

Fig. 23 shows the normalized simulated and measured radiation patterns in the *yz*-plane, which validates the beam-scanning ability of the antenna from +16° to +48° by increasing the frequency from 75 GHz to 95 GHz, as well as the measured co-polarized and cross-polarized radiation patterns. The deviation and squint of the measured beam compared with the simulation can be attributed to the manufacturing tolerance, inaccuracies in substrate permittivity, and measurement errors. For the radiation pattern measurements, two extenders (R&S ZC110 and ZRX110L), one for signal generation and the other for signal detection, characterize the beam profile between 75 GHz and 95 GHz. As shown in Fig. 21, the receiver has been installed on an automatic hemispherical goniometer system. A C-shaped sliding rail enables receiver movement over an inclination range of 0° to 50° in steps of 1° over an elevation range. A 360° rotation in the horizontal plane is carried out by another ring sliding rail in steps of 5° over the entire azimuthal plane.

Fig. 24 depicts the simulated and measured 3D realized gain patterns in the *yz*-plane across a frequency range of 75 GHz to 95 GHz with a step of 5 GHz. As frequency increases, the simulated beam scans from +16° to +44°, and the measured beam scans from +16° to +48°. An acceptable agreement emerges between the simulated and measured results. It should be noted that an accurate measurement of the far-field radiation pattern in the backward direction is not achievable in the area blocked by the GSG probe structure [44]. This blocked area is particularly notable near

TABLE 3. Comparison of the proposed millimeter-wave LWA with previously reported works covering similar frequencies within V- and W-bands.

Ref.	Type	Length	Technology	Bandwidth (FBW%)	Scanning Range	Max Gain (dBi)	Min RE	Max AE	Suppression
[23]	SIIG	$5.62\lambda_0$	LTCC	58-67 (14%)	$+7°$ to $+38°$	11.7	0.8	0.27	—
[23]	SIIG	$10.2\lambda_0$	LTCC	90-98 (8%)	$+23°$ to $+45°$	15	0.82	0.12	—
[24]	SIW	$16\lambda_0$	PCB	54-72 (28%)	$-28°$ to $+38°$	17 (sim)	0.6	0.25	OSB
[7]	MS + Patch	$18.8\lambda_0$	PCB	77.5-85.5 (9%)	$-19.5°$ to $-5°$	18	0.33	0.18	No
[9]	CRLH HMSIW	$5.6\lambda_0$	PCB	55-65 (16%)	$-72°$ to $+48°$	14.5	0.5	0.58	OSB
[10]	Slotted WG	$57\lambda_0$	Split-Block	84.8-109.3 (25%)	$+23°$ to $+44°$	26	N.A.	N.A.	—
[8]	IDW	$10.8\lambda_0$	3D printing	50-85 (51%)	$-9°$ to $+40°$	14.2	0.55	0.19	No
[36]	SSPP rod	$17.3\lambda_0$	3D printing	50-70 (33%)	$-39°$ to $-3°$	23.9	0.6	0.39	—
[37]	SSPP rod	$5.84\lambda_0$	3D printing	50-75 (40%)	near endfire	14.95	0.55	0.13	—
[25]	GCPW SIW	$10.25\lambda_0$	Photolithography	88-94 (6%)	$+42°$ to $+56°$	12.5	0.8	0.21	—
This work	**SSPP Q-GS**	$\mathbf{8.38\lambda_0}$	**Photolithography**	**55-95 (53%)** (sim) **75-95 (23%)** (meas)	**-30° to +46°** (sim) **+16° to +48°** (meas)	**15.9** (sim) **15** (meas)	**0.77** (sim)	**0.65**	**OSB, GL**

RE: Radiation efficiency, AE: Aperture efficiency, SIIG: Substrate integrated image guide; CRLH: Composite right left handed; MS: Microstrip; WG: Waveguide; HMSIW: Half-mode substrate integrated waveguide; IDM: Inset dielectric waveguide; Q-GS: Quasi-glide symmetry, GL: Grating lobe.

the antenna probe interface, where the interaction of EM waves can distort the desired radiation. To overcome this challenge, a parameter in the antenna design, indicated as the distance t in Fig. 5, plays a pivotal role. This parameter signifies the starting point of the parasitic patches with respect to the CPW, which is fed by the GSG probe. By increasing t, it may be possible to expand the measured radiation area beyond the GSG probe blockage. A modified GSG probe with an extended coaxial probe tip can also increase the distance between the probe body and the radiating region of the antenna, thereby reducing distortion and reflection caused by the probe and enabling more reliable characterization of the backward radiation region [46].

Fig. 25 shows the simulated maximum peak realized gain, directivity, aperture efficiency, and radiation efficiency from 55 GHz to 95 GHz, as well as the measured maximum peak realized gain from 75 GHz to 95 GHz. The simulated radiation efficiency of the proposed antenna is more than 0.77, from 55 GHz to 95 GHz. The aperture efficiency of our work is calculated using the formula $\eta_{ap} = \frac{D\lambda^2}{4\pi A}$, where D represents the directivity and A is the physical area of the overall antenna structure, including the transition section. The comparison between the simulated and measured maximum peak realized gain within the frequency range of 75 GHz to 95 GHz reveals an acceptable agreement. The observed gain reduction around 85 GHz may be attributed to the radiation loss originating from EM coupling from the flaring ground to the corrugations in the TC, as shown in Fig. 3. The simulations show a gain reduction at 85 GHz, while the measurements indicate a slight shift to 85.8 GHz. This discrepancy can be attributed to slight variations in substrate permittivity and fabrication imperfections, particularly small deviations in the slot offsets and slot widths introduced during photolithography and etching. One can notice a difference in the measured and simulated realized gain, which may be due to manufacturing errors and differences in conductor and dielectric losses of the materials in simulation and fabrication. These losses become more pronounced as the frequency increases. Higher-order modes might also deviate from theoretical expectations, leading to a gain reduction at higher frequencies.

In Table 3, the proposed LWA is compared to similar state-of-the-art millimeter-wave LWAs within V- and W-bands in terms of the implementation technique, radiator length, maximum peak realized gain, and beam-scanning ability. Compared to other LWAs, our antenna achieves a smaller radiator length while maintaining a high measured maximum peak realized gain of 15 dBi. The simulated beam-scanning range of our antenna is from $-30°$ to $+46°$ across the frequency range of 55 GHz to 95 GHz with suppressed OSB and grating lobe, while the measured beam-scanning range is from $+16°$ to $+48°$ over a frequency range of 75 GHz to 95 GHz. The limitations in the negative angular range are due to the shadowing effects of the GSG probe. The simulated radiation efficiency remains above 0.77 in the entire range of 55 GHz to 95 GHz. The maximum aperture efficiency of our work is 0.65. Moreover, compared with these published millimeter-wave LWAs, the unit cell of the proposed LWA can be designed to independently suppress the OSB and grating lobe issues by exploiting quasi-glide symmetry with asymmetrical slots in the structures.

VI. CONCLUSION

In this article, a millimeter-wave SSPP LWA with independent suppression of the OSB and grating lobe is designed, analyzed, and experimentally validated. A compact, low-loss, and broadband transition transfers the signal from the CPW to the SSPP-TL. Two rows of circular patches near the SSPP-TL operate as the radiation sections. Theoretical method and numerical simulations explain the frequency-dependent beam-scanning principle and predict the radiation pattern. The OSB is suppressed using quasi-glide symmetry in the antenna unit cell and analyzed by extracting the dispersion characteristics. Asymmetrical slots are exploited to suppress the grating lobe issue by tilting the unit cell radiation, which enhances radiation in the main beam direction and reduces it in the grating lobe region. According to full-wave simulations, the LWA has good radiation performance in a broadband from 55 GHz to 95 GHz with a scanning range of 76°, a maximum gain of 15.9 dBi, a minimum radiation efficiency of 77%, and a gain variation of 3.8 dB. The radiation section of the antenna occupies $6.8\lambda_0$, demonstrating good compactness. The fabricated LWA is experimentally validated in the 75-95 GHz range, demonstrating a scanning range from 16° to 48° and a maximum measured gain of 15 dBi. These results agree well with the simulations. The fabricated prototype on a fused silica wafer using photolithography would be an attractive candidate for millimeter-wave radar and imaging systems.

REFERENCES

[1] M. Steeg, M. Szczęsny, and A. Stöhr, "Multiuser 5G hot-spots based on 60 GHz leaky-wave antennas and WDM radio-over-fiber," in *Proc. ENRI Int. Workshop ATM/CNS (EIWAC)*, 2017, pp. 233–246.

[2] C. Dehos, J. L. González, A. De Domenico, D. Kténas, and L. Dussopt, "Millimeter-wave access and backhauling: The solution to the exponential data traffic increase in 5G mobile communications systems?" *IEEE Commun. Mag.*, vol. 52, no. 9, pp. 88–95, Sep. 2014.

[3] Y.-H. Chou, S.-J. Lin, and S.-J. Chung, "Analysis of a grating metal structure with broad back-scattering field pattern for applications in vehicle collision avoidance system," *IEEE Trans. Veh. Technol.*, vol. 51, no. 1, pp. 194–199, Jan. 2002.

[4] G. M. Brooker, "Mutual interference of millimeter-wave radar systems," *IEEE Trans. Electromagn. Compat.*, vol. 49, no. 1, pp. 170–181, Feb. 2007.

[5] M. T. Ghasr, S. Kharkovsky, R. Bohnert, B. Hirst, and R. Zoughi, "30 GHz linear high-resolution and rapid millimeter wave imaging system for NDE," *IEEE Trans. Antennas Propag.*, vol. 61, no. 9, pp. 4733–4740, Sep. 2013.

[6] V. Dyadyuk, J. D. Bunton, J. Pathikulangara, R. Kendall, O. Sevimli, L. Stokes, and D. A. Abbott, "A multigigabit millimeter-wave communication system with improved spectral efficiency," *IEEE Trans. Microw. Theory Techn.*, vol. 55, no. 12, pp. 2813–2821, Dec. 2007.

[7] A. E. Olk, M. Liu, and D. A. Powell, "Printed tapered leaky-wave antennas for W-band frequencies," *IEEE Trans. Antennas Propag.*, vol. 70, no. 2, pp. 900–910, Feb. 2022.

[8] X. Bai, S.-W. Qu, K.-B. Ng, and C. H. Chan, "Sinusoidally modulated leaky-wave antenna for millimeter-wave application," *IEEE Trans. Antennas Propag.*, vol. 64, no. 3, pp. 849–855, Mar. 2016.

[9] A. Sarkar and S. Lim, "60 GHz compact larger beam scanning range PCB leaky-wave antenna using HMSIW for millimeter-wave applications," *IEEE Trans. Antennas Propag.*, vol. 68, no. 8, pp. 5816–5826, Aug. 2020.

[10] D. A. Schneider, M. Rösch, A. Tessmann, and T. Zwick, "A low-loss W-band frequency-scanning antenna for wideband multichannel radar applications," *IEEE Antennas Wireless Propag. Lett.*, vol. 18, pp. 806–810, 2019.

[11] G. Lovat, P. Burghignoli, and D. R. Jackson, "Fundamental properties and optimization of broadside radiation from uniform leaky-wave antennas," *IEEE Trans. Antennas Propag.*, vol. 54, no. 5, pp. 1442–1452, May 2006.

[12] S. Paulotto, P. Baccarelli, F. Frezza, and D. R. Jackson, "A novel technique for open-stopband suppression in 1-D periodic printed leaky-wave antennas," *IEEE Trans. Antennas Propag.*, vol. 57, no. 7, pp. 1894–1906, Jul. 2009.

[13] S. Otto, A. Al-Bassam, A. Rennings, K. Solbach, and C. Caloz, "Transversal asymmetry in periodic leaky-wave antennas for bloch impedance and radiation efficiency equalization through broadside," *IEEE Trans. Antennas Propag.*, vol. 62, no. 10, pp. 5037–5054, Oct. 2014.

[14] U. Dey, J. Tonn, and J. Hesselbarth, "Millimeter-wave dielectric waveguide-based leaky-wave antenna array," *IEEE Antennas Wireless Propag. Lett.*, vol. 20, pp. 361–365, 2021.

[15] P. Padilla, L. F. Herrán, A. Tamayo-Domínguez, J. F. Valenzuela-Valdés, and O. Quevedo-Teruel, "Glide symmetry to prevent the lowest stopband of printed corrugated transmission lines," *IEEE Microw. Wireless Compon. Lett.*, vol. 28, no. 9, pp. 750–752, Sep. 2018.

[16] M. Bagheriasl, O. Quevedo-Teruel, and G. Valerio, "Bloch analysis of artificial lines and surfaces exhibiting glide symmetry," *IEEE Trans. Microw. Theory Techn.*, vol. 67, no. 7, pp. 2618–2628, Jul. 2019.

[17] G. Zhang, Q. Zhang, Y. Chen, and R. D. Murch, "High-scanning-rate and wide-angle leaky-wave antennas based on glide-symmetry Goubau line," *IEEE Trans. Antennas Propag.*, vol. 68, no. 4, pp. 2531–2540, Apr. 2020.

[18] P.-Y. Wang, Y.-L. Lyu, F.-Y. Meng, A. Rennings, and D. Erni, "Grating-lobe suppression for periodic leaky-wave antennas at the full array level," *IEEE Antennas Wireless Propag. Lett.*, vol. 21, pp. 2115–2119, 2022.

[19] W. Alshrafi, A. Al-Bassam, and D. Heberling, "Grating lobe mitigation in series-fed patch periodic leaky-wave antenna using parasitic monopoles," *IEEE Antennas Wireless Propag. Lett.*, vol. 19, pp. 2472–2476, 2020.

[20] W. Alshrafi, A. Al-Bassam, and D. Heberling, "Grating lobe reduction using tilted beam unit cell in series-fed patch periodic leaky-wave antennas," in *Proc. 15th Eur. Conf. Antennas Propag. (EuCAP)*, Mar. 2021, pp. 1–5.

[21] J. Liu, "Periodic leaky-wave antennas based on microstrip-fed slot array with different profile modulations for suppressing open stopband and n = -2 space harmonic," *IEEE Trans. Antennas Propag.*, vol. 69, no. 11, pp. 7364–7376, Nov. 2021.

[22] K. Wang, Y. Li, Z. Liang, S. Y. Zheng, and Y. Long, "A lateral scanning periodic leaky-wave antenna using reverse dipole pair element for suppressing-2nd space harmonic," *IEEE Trans. Antennas Propag.*, vol. 70, no. 12, pp. 12311–12316, Dec. 2022.

[23] Y. J. Cheng, Y. X. Guo, X. Y. Bao, and K. B. Ng, "Millimeter-wave low temperature co-fired ceramic leaky-wave antenna and array based on the substrate integrated image guide technology," *IEEE Trans. Antennas Propag.*, vol. 62, no. 2, pp. 669–676, Feb. 2014.

[24] K. Neophytou, S. Iezekiel, M. Steeg, and A. Stöhr, "Design of PCB leaky-wave antennas for wide angle beam steering," in *Proc. 11th German Microw. Conf. (GeMiC)*, Freiburg, Germany, Mar. 2018, pp. 152–155.

[25] D. Zelenchuk, A. J. Martinez-Ros, T. Zvolensky, J. L. Gomez-Tornero, G. Goussetis, N. Buchanan, D. Linton, and V. Fusco, "W-band planar wide-angle scanning antenna architecture," *J. Infr., Millim., THz Waves*, vol. 34, no. 2, pp. 127–139, Feb. 2013.

[26] J. Y. Yin, J. Ren, Q. Zhang, H. C. Zhang, Y. Q. Liu, Y. B. Li, X. Wan, and T. J. Cui, "Frequency-controlled broad-angle beam scanning of patch array fed by spoof surface plasmon polaritons," *IEEE Trans. Antennas Propag.*, vol. 64, no. 12, pp. 5181–5189, Dec. 2016.

[27] E. Farokhipour, N. Komjani, and M. A. Chaychizadeh, "An ultra-wideband three-way power divider based on spoof surface plasmon polaritons," *J. Appl. Phys.*, vol. 124, no. 23, Dec. 2018, Art. no. 235310.

[28] Q. Ma, H. Pu, A. Jin, R. Wang, and L. Liu, "A high-efficiency full-space scanning leaky-wave antenna based on SSPPs," *IEEE Antennas Wireless Propag. Lett.*, vol. 24, pp. 3759–3763, 2025.

[29] T. Wang, L. Liu, H. Ni, L. Zhu, and G. Q. Luo, "A full-angle scanning leaky wave antenna based on odd-mode SSPP from backfire to endfire," *IEEE Trans. Antennas Propag.*, vol. 71, no. 11, pp. 8570–8579, Nov. 2023.

[30] L. Ye, Z. Wang, J. Zhuo, F. Han, W. Li, and Q. H. Liu, "A back-fire to forward wide-angle beam steering leaky-wave antenna based on SSPPs," *IEEE Trans. Antennas Propag.*, vol. 70, no. 5, pp. 3237–3247, May 2022.

[31] E. Farokhipour, B. Sievert, J. T. Svejda, A. Rennings, N. Komjani, and D. Erni, "Wide-angle spoof surface plasmon polariton leaky-wave antenna exploiting prefractal structures with backfire to nearly endfire scanning," *IEEE Antennas Wireless Propag. Lett.*, vol. 21, pp. 2507–2511, 2022.

[32] S. Zohrevand, M. A. C. Zadeh, E. Farokhipour, D. Erni, and N. Komjani, "A small-aperture and high-performance endfire holographic antenna based on spoof surface plasmon polaritons," *IEEE Antennas Wireless Propag. Lett.*, vol. 23, no. 9, pp. 2743–2747, May 2024.

[33] E. Farokhipour, P.-Y. Wang, A. Rennings, and D. Erni, "Wide-angle SSPP-based leaky-wave antenna with scanning improvement in the forward quadrant for millimeter wave applications," in *Proc. 17th Eur. Conf. Antennas Propag. (EuCAP)*, Mar. 2023, pp. 1–4.

[34] Y. Zhang, H. Wang, and D. Liao, "A unidirectional beam-scanning antenna excited by corrugated metal–insulator–metal ground supported spoof surface plasmon polaritons," *IEEE Access*, vol. 7, pp. 36481–36488, 2019.

[35] S. Ge, Q. Zhang, C.-Y. Chiu, Y. Chen, and R. D. Murch, "Single-side-scanning surface waveguide leaky-wave antenna using spoof surface plasmon excitation," *IEEE Access*, vol. 6, pp. 66020–66029, 2018.

[36] Q. L. Zhang, B. J. Chen, K. F. Chan, and C. H. Chan, "High-gain millimeter-wave antennas based on spoof surface plasmon polaritons," *IEEE Trans. Antennas Propag.*, vol. 68, no. 6, pp. 4320–4331, Jun. 2020.

[37] Q.-L. Zhang, B.-J. Chen, Q. Zhu, K. F. Chan, and C. H. Chan, "Wideband millimeter-wave antenna with low cross polarization based on spoof surface plasmon polaritons," *IEEE Antennas Wireless Propag. Lett.*, vol. 18, pp. 1681–1685, 2019.

[38] L. P. Zhang, H. C. Zhang, Z. Gao, and T. J. Cui, "Measurement method of dispersion curves for spoof surface plasmon polaritons," *IEEE Trans. Antennas Propag.*, vol. 67, no. 7, pp. 4920–4923, Jul. 2019.

[39] J. Ren, H.-H. Zhang, C. Zhang, T. Yang, K.-D. Xu, and Y. Yin, "Accurate dispersion extracting and designing method for spoof surface plasmon polaritons leaky-wave antennas based on short and open calibration," *IEEE Trans. Circuits Syst. II, Exp. Briefs*, vol. 71, no. 6, pp. 2926–2930, Jun. 2024.

[40] M. A. Unutmaz and M. Unlu, "Spoof surface plasmon polariton delay lines for terahertz phase shifters," *J. Lightw. Technol.*, vol. 39, no. 10, pp. 3187–3192, May 2021.

[41] C. A. Balanis, *Antenna Theory Analysis and Design*, 3rd ed., Hoboken, NJ, USA: Wiley, 2005.

[42] F. Xu and K. Wu, "Guided-wave and leakage characteristics of substrate integrated waveguide," *IEEE Trans. Microw. Theory Techn.*, vol. 53, no. 1, pp. 66–73, Jan. 2005.

[43] B. Sievert, J. T. Svejda, D. Erni, and A. Rennings, "Spherical mm-wave/THz antenna measurement system," *IEEE Access*, vol. 8, pp. 89680–89691, 2020.

[44] B. Sievert, "Equivalent circuit-based efficiency enhanced on-chip antennas for wideband mm-wave radar systems," Ph.D. dissertation, Univ. Duisburg-Essen, Oct. 2023, doi: 10.17185/duepublico/81323.

[45] D. Titz, F. Ferrero, P. Brachat, G. Jacquemod, and C. Luxey, "Efficiency measurement of probe-fed antennas operating at millimeter-wave frequencies," *IEEE Antennas Wireless Propag. Lett.*, vol. 11, pp. 1194–1197, 2012.

[46] L. Boehm, M. Hitzler, F. Roos, and C. Waldschmidt, "Probe influence on integrated antenna measurements at frequencies above 100 GHz," in *Proc. 46th Eur. Microw. Conf. (EuMC)*, Oct. 2016, pp. 552–555.

EHSAN FAROKHIPOUR (Graduate Student Member, IEEE) received the B.Sc. degree in electrical engineering-communication from the Shahid Bahonar University of Kerman, Kerman, Iran, in 2015, and the M.Sc. degree in electrical engineering-electromagnetic fields and waves from Iran University of Science and Technology, Tehran, Iran, in 2018. From 2019 to 2021, he was a Research Assistant with the Millimeter-Wave Research Laboratory, Iran University of Science and Technology. Since 2022, he has been a member of the Laboratory for General and Theoretical Electrical Engineering, University of Duisburg–Essen. His research interests include the manipulation of EM waves, on-chip antennas, beam steering techniques, leaky-wave antennas, metasurfaces, and lens-based systems for millimeter-wave/sub-THz applications.

PENG-YUAN WANG received the B.E. degree in electronic and information engineering from Dalian Maritime University, Dalian, China, in 2014, the M.E. degree in electromagnetic field and microwave technology from Harbin Institute of Technology, Harbin, China, in 2016, and the Dr.-Ing. degree in electrical engineering from the University of Duisburg–Essen, Duisburg, Germany, in 2024. Since 2025, he has been an Assistant Professor with the Department of Electrical and Electronic Engineering, University of Nottingham Ningbo China (UNNC). His research interests include beam-steering antennas, leaky-wave antennas, and liquid crystal-based mmWave devices. He was recognized as an Outstanding Reviewer by IEEE ANTENNAS AND WIRELESS PROPAGATION LETTERS and IEEE OPEN JOURNAL OF ANTENNAS AND PROPAGATION and as a Top Reviewer by IEEE TRANSACTIONS ANTENNAS PROPAGATION.

BENEDIKT SIEVERT (Member, IEEE) was born in Krefeld, Germany. He received the B.Sc., M.Sc., and Dr.-Ing. degrees in electrical engineering from the University of Duisburg–Essen, Duisburg, Germany, in 2017, 2019, and 2023, respectively. From 2017 to 2023, he was a member of the Laboratory for General and Theoretical Electrical Engineering, University of Duisburg–Essen. In 2024, he joined the Department of Integrated Circuits, Fraunhofer Institute for High Frequency Physics and Radar Techniques (FHR), Wachtberg, Germany. His research interests include integrated circuits and on-chip antennas for mm-wave systems, as well as theoretical and computational electromagnetics.

ANDREAS RENNINGS (Member, IEEE) received the Dipl.-Ing. and Dr.-Ing. degrees from the University of Duisburg–Essen, Germany, in 2000 and 2008, respectively. He studied electrical engineering at the University of Duisburg–Essen.

From 2006 to 2008, he was with IMST GmbH, Kamp-Lintfort, Germany, where he was an RF Engineer. Since then, he has been a Senior Scientist and the Principal Investigator of the Laboratory for General and Theoretical Electrical Engineering, University of Duisburg–Essen. He carried out his Diploma work during a stay at the University of California, Los Angeles. His general research interests include the all aspects of theoretical and applied electromagnetics, currently with a focus on medical applications and on-chip millimeter-wave/THz antennas.

Dr. Rennings has received several awards, including the Student Paper Prize at the 2005 IEEE Antennas and Propagation Society International Symposium and the VDE-Promotionspreis 2009 for the dissertation.

DANIEL ERNI (Member, IEEE) received the Diploma degree in electrical engineering from the University of Applied Sciences Rapperswil (OST), Rapperswil, Switzerland, in 1986, and the Diploma degree in electrical engineering and the Ph.D. degree in laser physics from ETH Zürich, Zürich, Switzerland, in 1990 and 1996, respectively.

Since 1990, he has been with the Laboratory for Electromagnetic Fields and Microwave Electronics (IFH), ETH Zürich. From 1995 to 2006, he was the Founder and the Head of the Communication Photonics Group, ETH Zürich. Since October 2006, he has been a Full Professor with the Laboratory for General and Theoretical Electrical Engineering, University of Duisburg–Essen, Duisburg, Germany. From 2017 to 2018, he was with the Institute of Electromagnetic Fields (IEF), ETH Zürich, as a Visiting Professor. He is currently the Co-Founder of the spin-off company airCode, Duisburg, working on flexible printed RFID technology. His current research interests include optical interconnects, nanophotonics, plasmonics, ultra-sensitive optical biosensing, advanced solar cell concepts, optical and electromagnetic metamaterials, RF, mm-wave and THz engineering, chipless flexible RFIDs, biomedical engineering, bioelectromagnetics, marine electromagnetics, computational electromagnetics, multiscale and multiphysics modeling, numerical structural optimization, and science and technology studies (STS).

Dr. Erni is a fellow of The Electromagnetics Academy and a member of the Center for Nanointegration Duisburg–Essen (CENIDE), Materials Chain, the Flagship Program of University Alliance Ruhr, Electrosuisse, the Swiss Physical Society (SPS), German Physical Society (DPG), and the Optical Society of America (OPTICA).